Development of a 3D fractal cirrus model and its use in investigating the impact of cirrus inhomogeneity on radiation

Sarah Kew

August 2003

Submitted to the Department of Mathematics University of Reading in partial fulfilments of the requirements for the degree of Master of Science.

I confirm that this is my own work and the use of all material from other sources has been properly and fully acknowledged.

ABSTRACT

For the very first time, a 3D fractal cirrus cloud model is developed which is able to successfully represent the vertical as well as horizontal inhomogeneity of ice clouds observed by 94 GHz radar. Unique to the model are a 3D fall streak structure, an anisotropic grid spacing necessary to resolve the fall streak structure, a characteristic power-law break of scale indicative of the maximum scale of variability and anisotropic mixing in the horizontal plane. A constant e ective radius, ice crystal fall speed, and generating level are assumed and a lognormal distribution function for ice water content (IWC).

Initially a spectrally isotropic fractal field is created in Fourier space. Manipulations of the Fourier amplitudes and phases allow the observed 1D spectral slope and wind shear at each height to be reproduced. The fractal is scaled in real space such that the mean IWC and standard deviation of In(IWC) match those of the radar data. A threshold IWC defines the cloud edge.

An intriguing dependence of spectral slope on height is observed whereby the slope is constant at cloud top but steepens below the generating level, reaching values of around -3 at cloud base. This e ect is attributed to mixing at small scales due to the intersection of fall streaks, which could result from variable fall speeds in the presence of wind shear.

The e ect of wind shear and scaling exponent on shortwave and longwave top-of-atmosphere fluxes are investigated for a thin idealised winter cirrus cloud using the Edwards-Slingo radiative scheme. It is found that as the wind shear increases, the cloud radiative properties become closer to their plane-parallel values. Flattening the spectral slope increases the shortwave albedo and decreases the upwelling longwave radiation, increasing the tendency towards plane-parallel behaviour.

Contents

| 1 | Introduction | | |
|---|--------------|--|----|
| | 1.1 | Importance of clouds in the earth's radiation budget | 1 |
| | 1.2 | Representation of clouds in GCMs | 2 |
| | 1.3 | The GCM Albedo problem | 3 |
| | 1.4 | Cloud inhomogeneity | 5 |
| | 1.5 | Fractal models of stratocumulus | 6 |
| | 1.6 | GCMs and vertical structure of cirrus | 8 |
| | 1.7 | Observations of cirrus | 9 |
| | 1.8 | Development of a 3D fractal cirrus model | 10 |
| | 1.9 | Outline | 12 |
| 2 | Cirı | rus cloud geometry | 13 |
| | 2.1 | Definition of cirrus | 13 |
| | 2.2 | Cirrus morphology | 14 |
| 3 | Ana | alysis of Observations | 17 |
| | 3.1 | The Galileo Radar | 17 |
| | 3.2 | Using time as a horizontal dimension | 18 |
| | 3.3 | Z-IWC relation | 21 |

CONTENTS

List of Figures

| 1.1 | Albedo bias | 4 |
|-----|---|----|
| 2.1 | A photograph of cirrus uncinus | 15 |
| 2.2 | A conceptual model of cirrus uncinus | 15 |
| 3.1 | Radar reflectivity time-height section for 27 December 1999 | 18 |
| 3.2 | UM wind profile | 20 |
| 3.3 | UM temperature profile | 20 |
| 3.4 | 1D power spectrum | 23 |
| 3.5 | Determination of the outer scale | 24 |
| 3.6 | Spectral slope as a function of height | 26 |
| 4.1 | k-space geometry | 31 |
| 4.2 | Cross-sections in the k_x | |

| ST (| OF FIGURES | vii |
|------|--|-----|
| 4.9 | Changing the spectral slope | 42 |
| 4.10 | Steepening the spectral slope for anisotropic mixing | 43 |
| 4.11 | E ect of anisotropic mixing | 44 |
| 4.12 | Progression from a spectrally isotropic fractal to the 3D cirrus model | 45 |
| 4.13 | The full 3D field, with a section cut away | 46 |
| 4.14 | Verification of the generating level and fall streak geometry | 47 |
| 4.15 | Fall streak structures for various generating levels | 49 |
| 4.16 | A sample 1D power spectrum for the model | 50 |
| 4.17 | Comparison of the requested spectral slope to those produced by the | |
| | model | 51 |
| 4.18 | Testing the anisotropic mixing | 52 |
| 4.19 | A three dimensional view of the fall streaks | 53 |
| 5.1 | Sensitivity test for the upwelling LW flux | 58 |
| 5.2 | Verification of the empirical formula for SW albedo | 59 |
| 5.3 | Comparison of SW albedo calculation methods | 60 |
| | | |

Chapter 1

Introduction

1.1 Importance of clouds in the earth's radiation budget

The change and stability of the climate are intimately connected to the earth's radiation budget, in which clouds play a fundamental role (e.g. Sassen, 2001). Clouds, in turn, are believed to be regulated by climate. The cloud-climate feedback is of great potential importance. For example, clouds are the main controller of global albedo, the fraction of solar radiation which is reflected back into space (Salby, 1996). Cahalan *et al.* (1994) calculated that a 10% decrease in this reflectance could increase the earth's surface temperature by 5°C, producing a warming similar to that since the last ice age, or that expected from a doubling of CO₂. At present, the predicted change in global albedo for a future climate varies greatly between different General

2

Research has mainly focussed on the most spatially frequent cloud type, stratocumulus, which being low and optically thick, primarily cools the climate by reflecting solar radiation back out to space. In the last few decades (Sassen and Mace, 2001),

3

However, many theoretical studies have shown that significant errors can occur in ra-

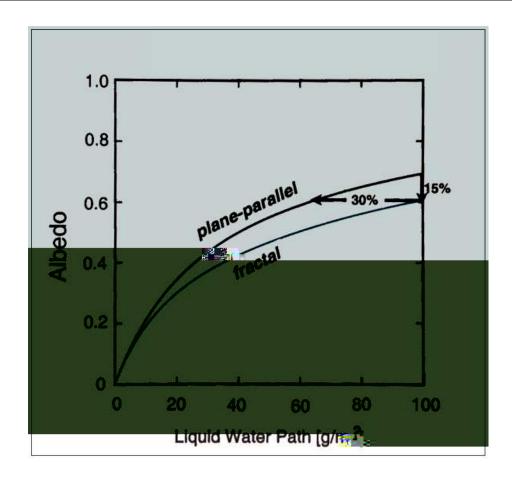


Figure 1.1: Dependence of albedo on mean liquid water path. The albedo for the fractal (inhomogeneous) case is computed from Cahalan's 'bounded cascade model' using the independent column approximation. When the liquid water path is 100 gm⁻², the bias is 15% of the plane-parallel albedo, and the mean reflectance equals that of a plane-parallel cloud with a water content reduced by 30% (after Cahalan, 1994).

portant to treat cloud radiation and hydrology consistently, as emphasised by Hogan and Illingworth, (2003). The longwave emissivity, which determines the outgoing longwave radiation is, similarly to albedo, a non-linear function of water path and is a ected by inhomogeneous structure of opically thin cloud (Pomroy and Illingworth, 2000). Other microphysical and macrophysical cloud processes are also a ected by

sub-grid scale structure (Larson *et al.*, 2001), but will have a di erent dependence on water path. Therefore, cloud parametrisations must take account of the sub-grid scale structure of clouds (Cahalan, 1994).

1.4 Cloud inhomogeneity

Much research has been done in investigating radiative transfer for 2D *horizontally* inhomogeneous clouds (e.g. Cahalan, 1994). Most GCMs now incorporate cloud

horizontal photon transport between columns (Cahalan, 1994). However, in the case of broken stratocumulus clouds, the ICA bias can be large (up to 30% due to side illumination, intercloud interaction and shadowing e ects) and even the sign of the bias is uncertain (Di Guiseppe and Tompkins, 2003).

1.5 Fractal models of stratocumulus

E orts to develop cloud resolving numerical models that resemble cloud observa-

presented supportive findings based on data from the FIRE (First ISCCP¹ Regional Experiment) programme. They showed that vertically integrated liquid water follows a $k^{-5=3}$ power-law, where k, the wavenumber, is the reciprocal of the length scale. An abrupt transition to smoother scaling behaviour occurs at scales less than a few 100 m. According to Davis *et al.* (1997), this break of scale is due to the mean photon path length between scattering events being approximately 100 m, and so below this scale, statistics derived from satellite radiance measurements are a ected. These smaller scales are reported not to have a significant e ect on large-scale albedo (Cahalan and Joseph, 1989).

Cahalan (1994) developed a very simple fractal model, known as the bounded fractal cascade, to obtain a linear log-log power spectrum of LWC with a spectral exponent of -5/3. Much has been brought to light from such models, such as the problem of albedo bias, but due to their unrealistic, inherently 'square' geometry, they are only really appropriate for overcast situations in which the ICA bias is minimal. The geometry also renders it di-cult to introduce realistic vertical structure, which often varies considerably from cloud-base to top (Di Guiseppe and Tompkins, 2003).

For realistic geometrical structure, we must turn to alternative techniques of generating fractal structure. One such approach is to specify scale invariance over a range of scales in Fourier space, and use inverse Fast Fourier Transforms (FFT) to produce the cloud field in physical space (e.g. Davis *et al.* (1997), Evans and Wiscombe (2003), Di Guiseppe and Tompkins (2003), Hogan and Illingworth (1999)). Incorporating wavenumber spectra into a fractal model is simple, at least when an isotropic grid spacing is used, and also carries additional properties, thought to be important e.g. a continuous size distribution and continuous scale invariance over a wide range of scales.

¹The 'International Satellite Cloud Climatology Project'.

Barker and Davies (1992) and Evans and Wiscombe (2003) presented stochastic models with horizontal spectral isotropy for boundary-layer clouds. In both cases, Fourier-filtering techniques were used to produce a spectral slope of cloud LWC based on observed values. In their 2D model of cumuloform clouds, Barker and Davies observed that as they steepened the scaling exponent, the distribution of cloud size in the field narrowed, the mean area of individual clouds increased, variability across individual clouds decreased and the albedo decreased. However no specific comment was made concerning the dependence and variability of parameters with height. This issue was raised by Cahalan and Joseph (1989). They went part-way to producing an answer for di erent boundary layer clouds by using Landsat satellite observations

scribed in chapter 2). Most cirrus clouds will span several vertical GCM grid boxes, which typically have vertical resolutions of 0.5 - 0.75 km at cirrus altitudes (Hogan and Illingworth, 2000). By good fortune, GCMs can go part-way in prescribing vertical structure when changes in the cloud fraction with height are translated by 'cloud overlap rules' into e ective horizontal variability of integrated cloud quantities, such as water path (Di Guiseppe and Tompkins, 2003). However, GCMs usually make the simplest assumption of maximum overlap between neighbouring cloudy layers (Hogan and Illingworth, 2000), resulting in moderately few possible cloud configurations (Pincus *et al.*, 2002). In nature, the same sized domains have substantially more horizontal variability and complicated vertical structure (e.g. Hogan and Illingworth, 2000). GCMs will therefore have to add some kind of representation of cloud inhomogeneity and its vertical correlation in future.

1.7 Observations of cirrus

Millimetre-wave radar is currently the sole remote sensing instrument that allows high-resolution observations of the vertical structure and properties of clouds in all types of conditions. Hogan and Illingworth (1999) simulated a 2D cirrus cloud field, using 1D spectral information obtained from radar observations at a specified height. They generated fields by performing the inverse Fourier transform of a 2D array containing 'wave amplitudes consistent with the energy at the various scales indicated by the 1D spectrum'. The spectral slope of their field was -2.16. Like all models mentioned here so far, their 2D fields were spectrally isotropic. Real cirrus clouds with fall streaks are, however, spectrally *anisotropic* in the horizontal, as fall streaks tend to be aligned parallel to the vertical wind shear. Previous models of cirrus containing fall streaks are limited. Danne *et al.* (1996) modelled the fall streaks of

cirrus as a series of idealised, sinusoidal 'cloud cells' in the x_i z plane, assuming the pattern to be constant in the y direction. The model served a purpose of validating a particular theory rather than advancing cirrus research. The spectra plotted in figure 4 of their paper suggest spectral slopes of -3.5 and -2.4. They acknowledged that further aspects should be accounted for in 2- or 3- dimensions, such as the tilting structure of the fall streaks due to vertical wind shear, or temporal and spatial changes of the wind direction. Whilst it is not possible to model the spatial changes in the wind profile using the Fourier technique, implementing the tilting of the fall streaks should be fairly straight forward.

1.8 Development of a 3D fractal cirrus model

No attempt has yet been made to create a 3D stochastic model of cirrus, and as of yet no suitable observations in 3D exist. In this study we develop a 3D fractal cirrus cloud model, which has realistic horizontal and vertical structure based on 2D (height-time) radar observations. The model will produce a 3D field of IWC which can be presented to radiation schemes in order to assess the e ect of the inhomogeneity and characterise the vertical structure of cirrus on radiative transfer. In addition, the model could be used as a tool in the interpretation of cirrus measurements in a 2D plane, for example, plan-view images from satellite or vertical cross-sections from ground based or spaceborne (following the launch of CloudSat in 2005 (Stephens *et al.*, 2002)) radar. Implemented in our model are the new aspects of three-dimensionally resolved fall streak geometry for any wind shear situation, anisotropic horizontal scaling and variation of power-law slope with height. The power-law for each height is wavenumber-dependent, with a cut-o applied at the wavenumber corresponding to the largest observed scale length. It is also possible to include a change in slope at

a characteristic wavenumber. The IWC for each height is scaled such that the mean IWC and standard deviation of In(IWC) are matched to the radar observations.

The grid resolution is equal for the two horizontal dimensions but is greater in the vertical. The adaptations of the Fourier method made to achieve this anisotropic spacing are specific to this study and di erent to that considered (but not applied 1.9 Outline

The Edwards-Slingo 1D radiative transfer code (Edwards and Slingo, 1996) is employed to assess the e ect of di erent scenarios (e.g. di erent wind shears) on the long-wave and short-wave radiative fluxes. For this we assume the ICA. The ICA is a strong assumption, justified by Cahalan (1994) for stratocumulus mesoscale domain-averaged fluxes, by the finding that flux increase and decrease due to horizontal transport tend to approximately cancel each other over the total area. To investigate the validity of the ICA for cirrus it would be necessary to perform a full 3D radiative transfer calculation. It would be interesting to observe how horizontal photon transport is a ected by fall streak orientation, but the required code is not yet ready for use. If significant results are obtained from the full-3D calculation, they will be reported elsewhere.

1.9 Outline

The next section provides a description of cirrus with particular reference to the fall streak geometry. Sections 3 and 4 describe the analysis of the radar data and the generation of the 3D fractal cirrus model respectively. Together they comprise

Chapter 2

Cirrus cloud geometry

Here we give a brief description of cirrus, for the purpose of introducing some of the concepts and terminology which will feature in later sections.

2.1 Definition of cirrus

Clouds are o cially classified by morphology. The internationally agreed definition of cirrus clouds, given by the World Meteorological Organisation (WMO), is:

Cirrus (Ci): Detached clouds in the form of white, delicate filaments or white or mostly white patches or narrow bands. These clouds have a fibrous (hair-like) appearance, or a silky sheen or both.

Cirrocumulus (Cc): Thin, white patch, sheet or layer of cloud without shading, composed of very small elements in the form of grains, ripples, etc., merged or separate, and more or less regularly arranged; most of the elements have an apparent width of less than one degree.

Cirrostratus (Cs): Transparent, whitish cloud veil of fibrous (hair-like)

or smooth appearance, totally or partially covering the sky, and generally producing halo phenomena.

Cirrus forms in the upper troposphere and most frequently occurs in layers or sheets with horizontal dimensions up to thousands of kilometres (Heymsfield and Mcfarquhar, 2001). Lynch (2001) suggested that perhaps the most significant physical property of cirrus (to which some of the qualities listed above are attributed) is that they are made mostly or completely of ice, which means that the cloud temperature is likely to be well below freezing. Homogeneous nucleation of ice crystals will occur if the temperature is less than i 41°C. Ice crystals are normally larger in size than water droplets and therefore they have greater fall speeds. This is the one of the main factors determining cirrus cloud geometry.

2.2 Cirrus morphology

Heymsfield (1975) developed concepts to explain the form of *cirrus uncinus*, a particular species of cirrus which exists almost exclusively in regions of wind shear. Cirrus uncinus are usually observed to be composed of a compact growth region, which we will refer to as the 'generating cell', and a trail of precipitating ice crystals, which we will refer to as the 'fall streak' (Starr and Quante, 2001). Heymsfield (1975) noted that trails without heads are quite frequently observed, and it can then be assumed that the cloud is in a decaying stage. Typically, the generating cell has a width of order 1km, and a thickness between 0.3 - 1.0 km (see figure 2.2 and also figure 2.1). Its appearance is similar to a lower cumuliform cloud. Individual cells can consist of groups of smaller updrafts and they have also been observed in mesoscale uncinus complexes with dimensions of up to thousands of kilometres.

Heymsfield (1975) reported that for development to begin, some slight instability



Figure 2.1: A photograph of cirrus uncinus. \bigcirc Pekka Parviainen (used with permission.)

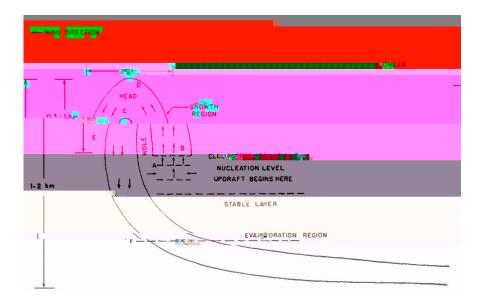


Figure 2.2: Conceptual model of the cirrus uncinus cloud for positive wind shear, showing the characteristic shape, dimension, and dynamical processes (after Heymsfield (1975)).

is necessary in order to initiate convection and updrafts. In addition, the relative humidity must be high enough for nucleation to occur (figure 2.2 level A). Once formed, the crystals grow rapidly and continue moving with the updraft (figure 2.2 level B). As the crystals grow, their fall speed will increase and at some point they will start to fall down through the updraft and become part of the fall streak.

Cirrus fall streaks may curve irregularly or slant sometimes with a comma shape as a result of the changes in horizontal wind velocity with height and variations in

Chapter 3

Analysis of Observations

This section describes how radar data on which the model is based is analysed. The radar data are used to characterise all the relevant properties of cirrus that we wish to capture in our model. The characteristics considered are spectral properties and their height dependence, the mean and spread of IWC at each height, and the fall streak structure. The simulations will use a 128 £ 128 £ 32 point grid. The horizontal dimensions of the domain, x and y, are both chosen to be 200 km, whilst the vertical dimension, z, is 5 km. This gives a resolution of 1562.5 m in the horizontal and 156.25 m in the vertical. These dimensions and resolutions apply to all figures, in this section and the next, unless otherwise stated.

3.1 The Galileo Radar

The observations from which the cloud model statistics are derived are obtained from Galileo, a 94 GHz, 0.45 m diameter cloud radar located at Chilbolton in the South of the UK. The radar is vertically pointing and operates with a pulse width of 0.5 7 s. The radar reflectivity factor Z is averaged over 30 second periods and is recorded for

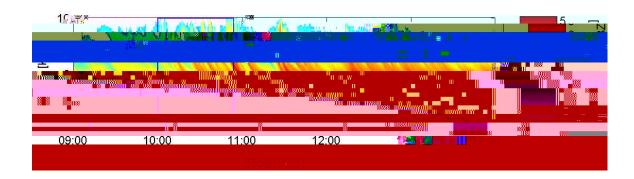


Figure 3.1: The time-height section of radar reflectivity recorded by Galileo on 27 December 1999.

a range of heights with a vertical resolution of 60 m. As clouds are advected across the radar, two-dimensional time-height fields of Z are built up. The units of Z are mm⁶m⁻³ but in this study, and normally in the literature, Z is referred to in dBZ, i.e. $10 \log_{10}(Z[\text{mm}^6\text{m}^{-3}])$.

The data on which this model is developed were recorded on 27 December 1999. The time-height reflectivities, for 09:00 UTC to 14:00 UTC, are illustrated in figure 3.1. This particular case of cirrus was chosen because the wind shear was ideally aligned with the direction of advection over the radar, resulting in complete fall streaks lying entirely within the time-height plane of the radar.

3.2 Using time as a horizontal dimension

The cloud structure depicted in radar imagery is not strictly equivalent to snapshots of the entire cirrus cloud field because of temporal alterations that occur in the clouds as they advect over the radar. However, the resultant changes are probably not major. Generally speaking, cirrus cloud elements develop more slowly than they advect in the relatively rapid transport of the upper troposphere (Sassen, 2001). The time

dimension is converted to horizontal distance using the assumption that the cloud moves with speed equal to the wind speed at the generating level (Marshall, 1953). Evans $et\ al.$ (2001) also used this approach. The height of the generating level can be directly but subjectively determined if generating cells can be seen in the Z cross-section. Otherwise, an informed guess can be made from the temperature profile. Temperature soundings of cirrus generating cells by Heymsfield (1975) indicated stable layers above and below the cell, whilst the cell itself was in a region with a dry adiabatic lapse rate. Typically generating cells are about 1 km thick (see figure 2.2), so if the temperature profile were unavailable, a crude approximation of 1 km below the cloud top for the generating level height could be made. The estimation can be refined in the simulation phase, by comparing the model's fall streak pattern with the observed pattern (see section 4.8.1).

In this study, wind component and temperature profiles are supplied by the mesoscale version of the Met O ce Unified Model (UM) forecasts for the relevant hour and date. If the time dimension of the cloud spans several hours, averaged profiles can be used. The data are interpolated appropriately for the vertical dimensions of the cloud. The u and v components (i.e. the components in the West-East and South-North directions respectively) of the wind profile for the cloud in figure 3.1 at 11:00 UTC are shown in figure 3.2. The wind shear is approximately 0.04 s⁻¹, in the region of the fall streaks.

Inspection of figure 3.1 and the temperature profile (figure 3.3) suggest that the generating level is at about 8 km, which is verified to be acceptable. The wind speed at 8 km is about 61.9 ms⁻¹, hence the 5-hour time span of the cloud shown translates to a horizontal distance of about 1100 km. The blue box encases the 200 km stretch of cloud chosen for analysis. The corresponding time period is about 54 minutes. This

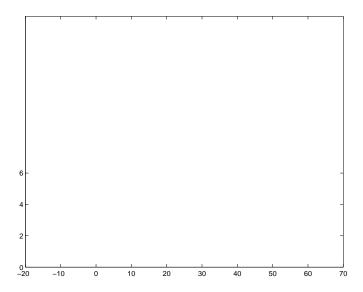


Figure 3.2: The UM wind profile at 11:00 UTC on 27 December 1999.

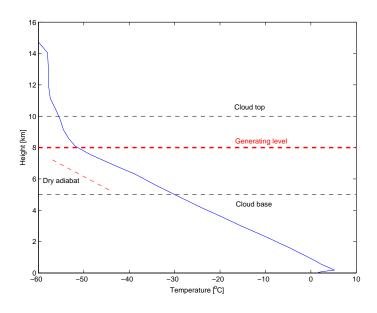


Figure 3.3: The UM temperature profile at 11:00 UTC on 27 December 1999.

3.3 Z-IWC relation 21

particular section was chosen because the cloud base is relatively flat. The horizontal domain size of 200 km encompasses the largest horizontal scale of variation (which we will see later is about 60 km).

3.3 Z-IWC relation

In order to compare the output of the model with those from other models, and also to be able to run a radiation scheme over the cloud, the cloud field should be defined using universal physical units (LWC or IWC), rather than units such as radar reflectivity, which are specific to the observation method used.

A 2D time-height field of Ice Water Content (IWC) is computed from the radar reflectivity factor ($\it Z$

certain wavenumber, which we will designate k_{outer} , the spectral slope tends to zero. The wavenumber k_{outer} , or rather its inverse, indicates an upper limit to the scale of structure within the cloud. We refer to this limit as the 'outer-scale'. A line of best-fit (black trace), obtained by section averaging, is plotted through the spectrum. In figure 3.5 we plot the lines of best-fit obtained from every third height range-gate. It can be seen that the change in slope occurs approximately at $k = 1.7 £ 10^{-5} m^{-1}$ for all heights, so we assign this value to k_{outer} , which corresponds to a horizontal 'outer scale' of about 60 km.

Figure 18 (b) in Hogan and Illingworth (1999) shows a cirrus power spectrum from

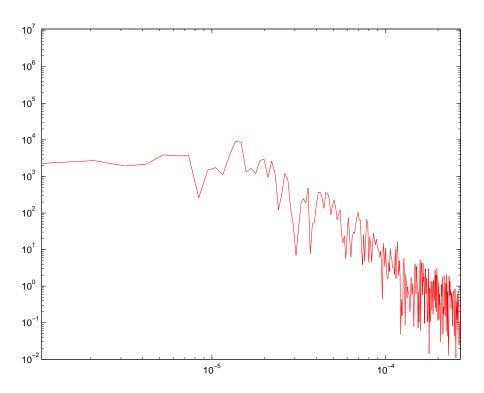


Figure 3.4: The 1D power spectrum (red trace) of the logarithm of IWC at a height of 5.91 km. A smoothed spectrum (black line) is obtained by averaging over equal sections of $\log k$. A least squares regression (blue dashed line) is used to determine the spectral slope, which for this case is i 2.9.

the method of obtaining a fit to the linear section of the power spectra (it can be seen in figure 3.4 that the slope is slightly underestimated, which is generally the case for all the observed spectra). Spectral exponents are well known to be di-cult to estimate, and often require many (or large-sized) samples (Tessier, 1993). This is why we use a large domain length to estimate the spectral characteristics of the cloud. Moving vertically downwards, the slope generally steepens, indicating that horizontal inhomogeneity is preferentially suppressed at smaller scales. In the figure we see that the slope starts to decrease at a height of about 8 km, which is the

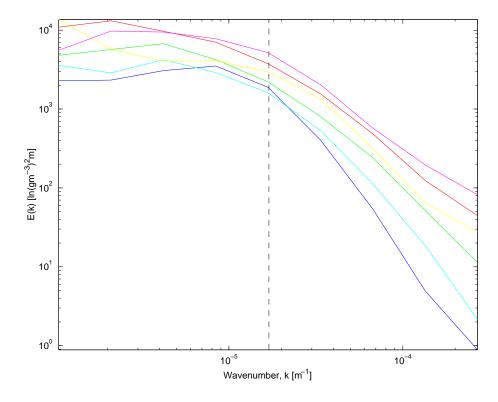


Figure 3.5:

3.5 Removal of white noise

Towards the cloud-top and cloud-base, the slope appears to flatten towards zero. This is a consequence of the system noise becoming comparable or greater than the radar reflectivity from the very low ice crystal concentrations in these regions. This led to gaps in the data which were dealt with by removing them and compressing the data. Consequently, towards the cloud base and cloud top, the spectral slope is shallower than we expected it to be. This e ect needs to be eliminated from the model as it has no physical significance. We assume that the slope remains at its minimum value towards the cloud base, and tails o at cloud top (to around i 3=2) as indicated in figure 3.6 by the dashed red line.

3.6 Calculation of mean and standard deviation of IWC for each layer

In order to estimate the true statistics of the cloud, the underlying probability density function (PDF) of IWC needs to be modelled. In this study we assume a lognormal distribution for IWC. The use of a lognormal PDF for water content has been suggested and used by Cahalan *et al.* (1994), Evans and Wiscombe (2003), and Hogan and Illingworth (2003). Cahalan *et al.* (1994) graphed the one-point PDF of Liquid Water path for stratocumulus and overplotted a lognormal with the same mean and variance, finding it to be a good fit. Evans and Wiscombe (2003) also stated that the PDF of LWC is usually close to being lognormal. Research by Hogan and Illingworth (2003) on ice clouds has shown that a lognormal PDF is a good fit for many IWC observations. The PDF for IWC is a flexible feature of this model and so a di erent function, even the exact PDF could be used. This was the approach taken by Evans

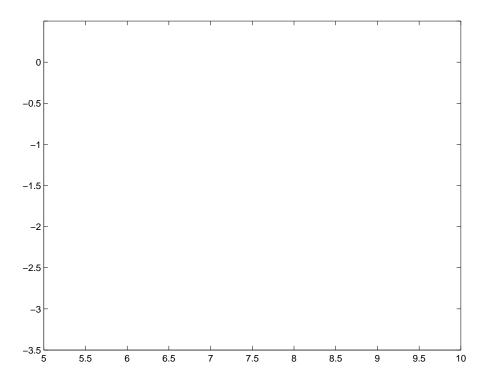


Figure 3.6: Spectral slope as a function of height of power spectra derived from the cirrus cloud observed in figure 3.1. The blue line shows the original analysis of In(IWC) obtained from the radar reflectivity. Fluctuations are smoothed by averaging over every 7 points of height (black line). The red-dashed line is the fit used in the model to give the spectral slope at each height.

and Wiscombe (2003). They transformed a Gaussian field to one having the observed LWC PDF using a lookup table.

In this study, the specific lognormal applied to a particular layer is defined by the mean IWC and the standard deviation of In(IWC). These are the statistics which we extract from the radar data at each vertical discretisation and use to scale the fractal lognormal IWC field produced by the model.

The limited sensitivity of the radar imposes a range dependent lower limit Z_c on

Chapter 4

Generation of the 3D model

This section outlines how the 3D fractal cloud field of IWC is generated using the radar analysis. The principle is that, for a particular height, a 1D Fourier analysis of the data yields a power spectrum with information about the structure at various scales at that same height. Then this information is used to simulate a 3D power spectrum. An inverse 3D FFT is applied to produce a 3D fractal with the same 1D power spectral properties as the radar data (if a power spectrum is taken across it).

The 3D model is partly based on adaptations from an existing but much simpler 2D fractal 'Fourier' model for cirrus cloud fields. The 2D model uses equal grid spacing in the x and y directions and produces a spectrally isotropic square field with fractal characteristics and zero mean. Each component of the Fourier matrix is a random complex number with a Gaussian distribution and a mean amplitude proportional to the square-root of the mean spectral energy. The spatial field is obtained by performing the inverse Fourier transform of the Fourier matrix and selecting the real part. Unique to the 3D model are the mani8h- mdel

4.1 The 3D wavenumber array

We require a 3D fractal field, f(x; y; z), consisting of $N_x \not\in N_y \not\in N_z$ points, with grid spacing x, y and z in the x, y and z directions respectively. We begin by creating the 3D wavenumber array k, which has the same dimensions as the fractal field. The maximum wave number in the

structures at cloud top, for example. In the scope of this work such complexities are neglected.

The one-dimensional energy spectrum is of the form

$$E_1(k) = \hat{E}_1 k^{\prime}; {4.1}$$

where k is the wavenumber, E_1 is the 1D spectral energy density, \hat{E}_1 is a constant related to the y-axis intercept on a log-log E(k) plot, and 1 is a constant equal to the gradient of the log-log E(k) plot.

Let us firstly consider the case for isotropic grid spacing (x = y = z). The continuous 3D spectral energy density, E_3 , may then be defined in terms of k, using the constraint that, at a particular wavenumber, E_1 is equal to the integral of E_3 over all directions for the same wavenumber:

$$E_{1}(k) = \int_{A=0}^{Z} \int_{\mu=1/4}^{A=2/4} E_{3}(k) k^{2} \sin \mu \, d\mu \, dA; \qquad (4.2)$$

where μ is the zenith angle and A is the azimuthal angle (see figure 4.1). In going from 1D to 3D space, the dependence on k becomes much steeper, but this ensures that the 1D power spectrum through resulting 3D field will have the correct slope. Equation 4.2 is evaluated and rearranged to give

$$E_3(k) = \frac{E_1(k)}{4 \frac{1}{4} k^2} = \frac{\hat{E}_1 k^{1-2}}{4 \frac{1}{4}}.$$
 (4.3)

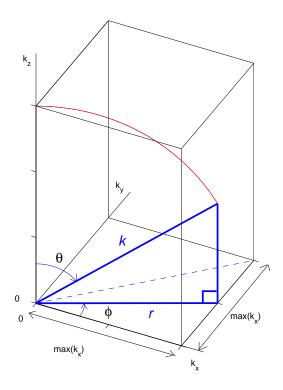


Figure 4.1: The geometry employed in k-space. Here μ is the zenith angle and \acute{A} is the azimuth. We define r to be the horizontal component of k when the k-vector just contacts the boundary of the domain. The dashed line marks the upper limit of \acute{A} at $\frac{1}{4}$ =4, which is applied when using anisotropic grid spacing.

k-space domain. So, E_3 is larger than it should be. This applies to large k only and here is assumed not to have a significant e ect.

If, however, the grid spacing is not isotropic, i.e. $x = y \lambda z$, equation

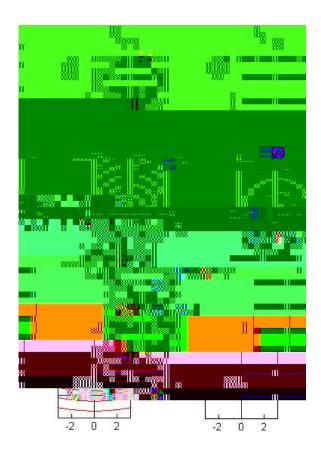


Figure 4.2: Cross-sections in the k_x - k_z plane at k_y =0.. The plotted range of k_x is j max(k_x) to + max(k_x), while the range of k_z is j max(k_z)=2 to + max(k_z)=2. The grid points have a large separation, k_z , in the k_z direction, but in the k_x direction they are so closely spaced that they have merged into (blue) solid lines (a): Intersection of k-shells with the k_x - k_z plane. Complete shells exist only when $k < \max(k_x)$. (b): Intersection of the shells $k = \max(k_x)$ (black), $k = k_z$ (green) and $k = k_z$ =2 (red) with the k_x - k_z plane.

When $k > \max(k_x)$, significant portions of the k-shell fall outside of k-space domain (see figure 4.2). To obtain the 'correct' spectral energy density relation equation for this range of k, we therefore need to change the limits on the integral over μ in equation (4.2). This analysis ensures that vertical power spectra of the simulated fractal have the correct spectral slope for scales smaller than x.

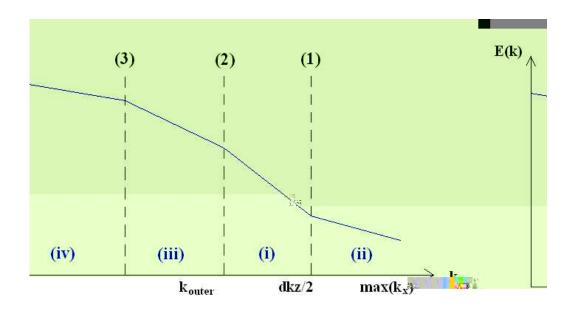


Figure 4.3: Schematic illustrating the di erent regimes of the 3D power spectrum. The spectral slope in region (i) remains unchanged. In region (ii) we apply the new equation (4.8). This reverts back to give the spectral slope in (i) at boundary (1) so a boundary condition does not have to be determined. In region (iii) we apply the 2D inner spectral slope and a constant of proportionality, A, is required to satisfy continuity at boundary (2). In region (iv) we apply the 2D outer spectral slope and a second constant of proportionality, B, is required to meet the boundary conditions at (3).

We use $\mu' = \mu'(k; A)$ to represent the upper limit of μ , which is attained when the k-vector makes contact with the surface of the cuboid. The μ' will be dependent on both wavenumber and the azimuthal angle, A (see figures 4.1 and 4.4). Due to the symmetry of the geometry, only one sixteenth of the k-sphere need be considered. We consider the upper hemisphere with azimuthal range of $0 < A < \frac{1}{2} = 4$. We integrate equation 4.2 over the new limits of $0 < A < \frac{1}{2} = 4$ and $0 < \mu < \mu'(k; A)$ and then multiply the result by a factor of 16.

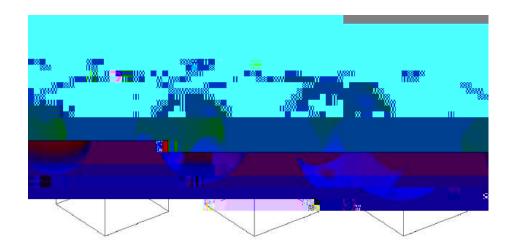


Figure 4.4: The μ dependence of the integration surface. Diagram (a) illustrates the k-shell within the domain of integration when $k < \max(k_x)$, in (b) is the relevant shell shape for $\max(k_x) < k < \frac{P}{2}\max(k_x)$, and (c) applies to all $k > \frac{P}{2}\max(k_x)$.

$$E_{1}(k) = 16 \int_{0}^{Z} \frac{1}{16} \int_{0}^{2} E_{3}(k)k^{2} \sin \mu d\mu dA \qquad (4.4)$$

$$= 16k^{2}E_{3} \int_{0}^{2} 1 \cos \mu dA \qquad (4.5)$$

Now, we can calculate $\cos \mu'$ using the geometry shown in figure 4.1:

$$\cos \mu = \frac{\rho_{\overline{k^2} i r^2}}{k};$$

where $r = \max(k_x) = \cos A$. Substituting for r, we insert this relation into equation (4.4) and obtain

$$E_1(k) = 16k^2 E_3 \int_0^{Z_{M=4}^3} 1_j \frac{Q_{M=4}^3}{1_j (\max(k_x) = k \cos A)^2} dA$$
: (4.6)

Rearranging (4.6), we find the 3D spectral energy density as a function of the 1D

spectral energy density,

$$E_{3}(k) = \frac{\frac{1}{16k^{2}} \frac{1}{0} \frac{E_{1}(k)}{1 \cdot i \cdot i} \frac{E_{1}(k)}{1 \cdot i \cdot i \cdot i} \frac{E_{1}(k)}{1 \cdot i \cdot i \cdot i} \frac{(4.7)}{1 \cdot i \cdot i} \frac{E_{1}(k)}{1 \cdot i \cdot i} \frac{1}{0} \frac{E_{1}(k)}{1 \cdot i \cdot i} \frac{1}{0} \frac{1}{1 \cdot i \cdot i} \frac{1}{0} \frac{E_{1}(k)}{1 \cdot i \cdot i} \frac{1}{0} \frac{1$$

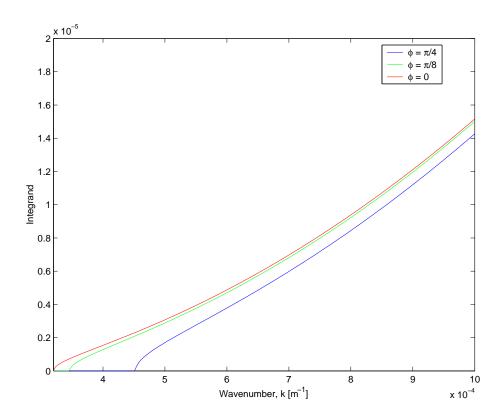


Figure 4.5: The smooth integrand of equation 4.8. The three di erent lines show the behaviour of the integrand for three di erent values of \vec{A} as indicated by the key.

points are contained within the k

Figure 4.6: Limits of the two spectral energy equations, 4.3 and 4.7, for large k. Equation 4.3 tends to the limit of $2\frac{1}{4}(\max(k_x))^2$ and the new equation 4.7 tends to the limit of $8(\max(k_x))^2$

constant of proportionality contains the factor $\frac{E_1}{4\%}$). Equating these two expressions at $k = k_z = 2$ and rearranging, we find,

$$A = \frac{\tilde{A}}{2} \frac{k_z! - \frac{13D_+}{i} \frac{12D}{i}}{2}$$
 (4.10)

In the radar analysis, a change of slope of the 1D power spectrum from 1 to 0 was seen to occur at $k=k_{outer}$. To implement this observation, we set the 3D spectral slope to $^{12D}_{o}=j$ 1, which is equivalent to setting the 1D spectral slope to 0, for all $k< k_{outer}$. To ensure continuity, we again apply a boundary condition, this time at

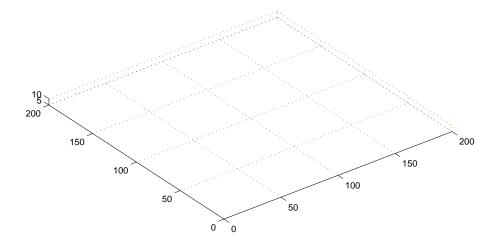
 k_{outer} . Now, for $k > k_{outer}$, we have $E_3 \nearrow A(k_{outer})^{-\frac{12D}{l}}$, and for $k < k_{outer}$ we have that $E_3 \nearrow B(k_{outer})^{-\frac{12D}{o}}$, where B is a second constant of proportionality. Equating these at $k = k_{outer}$ we find,

$$B = A (k_{outer})^{-\frac{12D}{i} + \frac{12D}{o}}; (4.11)$$

To summarise, the spectral energy density matrix is described in four parts (see figure 4.3), according to the magnitude of the wavevector:

$$E_{3} = \frac{E_{1}}{4 \frac{1}{4}} E \begin{cases} 8 & k^{-\frac{12D}{o}} & k < k_{outer} \\ A & k^{-\frac{12D}{i}} & k_{outer} < k < k_{z} = 2 \\ k^{-\frac{13D}{i}} & k_{z} = 2 < k < \max(k_{x}) \\ \frac{1}{i} & k^{-\frac{13D}{i}} & k > \max(k_{x}); \end{cases}$$

where
$$A = \frac{\tilde{A}}{2} \frac{k_z! - {}^{13D} + {}^{12D}}{2}$$
; $B = A(k_{outer})^{-\frac{12D}{i} + \frac{12D}{o}}$
and $I = 1_i = \frac{4}{\frac{1}{4}} \frac{\frac{7}{4}}{0} \frac{1_i (\max(k_x) = k \cos A)^2}{1_i (\max(k_x) = k \cos A)^2} dA$:



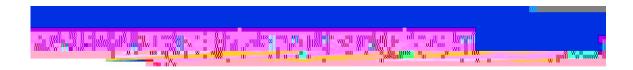


Figure 4.8: Illustration of the wind shear simulation for a vertical cross-section of the 3D cloud field of length 200 km and a vertical dimension of 5 km.

fall streaks in this way, due to periodicity of the field. Above the generating level $\pm x = \pm y = 0$; i.e. we make the simplifying assumption that there is no shear in the generating cell, which is not always the case (Heymsfield, 1975).

4.5 Perturbation of Fourier amplitudes: Isotropic mixing

From the analysis of the radar data, we saw that the spectral slope was a function of height. To simulate the same variation with height, we need to perturb the Fourier amplitudes.

The fractal field is divided into N_z horizontal slices, each of depth z. Each slice is transformed back into the Fourier domain for manipulation, using the 2D Fourier transform. The Fourier components are multiplied by the *square root* of the required change in energy density, since we are in amplitude space, i.e. $k^{(new slope-old slope)=2}$, where $k = \frac{q}{k_x^2 + k_y^2}$ defines the 2D wavenumber. If the slope becomes more shallow, this will have the e ect of amplifying the small-scale structure and suppressing the large (figure 4.9). Similarly if the slope becomes steeper, the converse applies. Finally, a 2D inverse Fourier transform is performed on each slice to obtain the new translated and spectrally filtered fractal field.

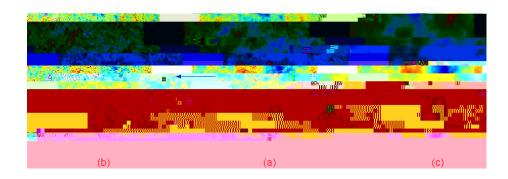


Figure 4.9:

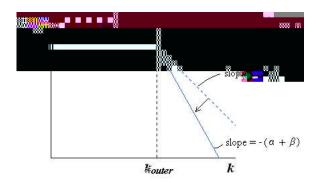


Figure 4.10: Steepening the spectral slope to achieve the required scaling exponent. If ® is the original slope and we request a slope of ® + $^-$, then the Fourier amplitudes are raised to the power of $^-$ =2. A scale factor of $(1=k_{outer})^{-}$ =2 enforces continuity at $k=k_{outer}$.

parallel to the direction \tilde{A} :

$$k_{\tilde{A}} = k_x \sin \tilde{A} + k_y \cos \tilde{A}. \tag{4.13}$$

To steepen the spectral slope from $k^{-(@)}$ to $k^{-(@+-)}$ (illustrated in figure 4.10), the complex Fourier coe cients are multiplied by a factor f where

$$f = \begin{cases} 8 \\ \langle jk_{\tilde{A}}j = k_{outer} \rangle^{-2} & \text{for } jk_{\tilde{A}}j > k_{outer} \\ > 1 & \text{for } jk_{\tilde{A}}j < k_{outer} \end{cases}$$

In this way, the spectrum is continuous at k_{outer} and no mixing is applied to scales larger than the outer scale. Anisotropic mixing is applied only to layers below the generating level, assuming that it is the fall streaks which generate the anisotropy. Above the generating level, isotropic mixing is required, as before, in order to obtain the observed spectral slope. Figure 4.11 illustrates the e ect for two di erent wind shear direction scenarios on a single layer.

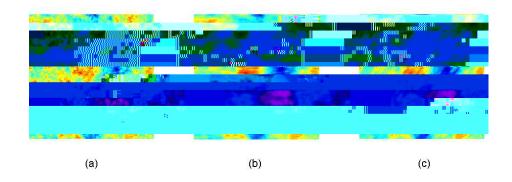


Figure 4.11: E ect of anisotropic mixing. Image (a) shows a slice of the original fractal field with a spectral slope of i 5=3. In (b), the spectral slope has been decreased by 1 in the E-W direction. In (c), the spectral slope has been decreased by 1 with respect to the spectral slope in (a) but in the SW-NE direction.

4.7 Scaling the fractal

The fractal field is treated as a field of In(IWC) and is scaled to obtain the required standard deviation of In(IWC) observed by the radar at each level. It is then exponentiated, to obtain a field of IWC, and scaled to achieve the required mean IWC at each level. This ensures that the IWC field has a lognormal distribution with the required mean and spread, see figure 4.12.

45



Figure 4.12:

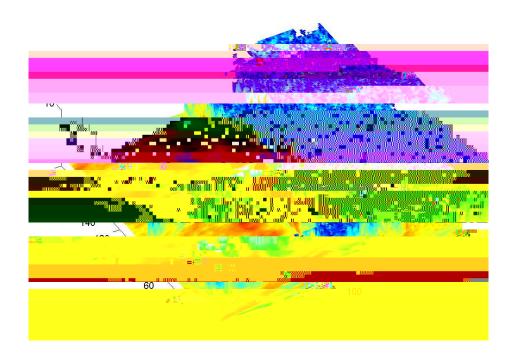


Figure 4.13: The full 3D field of In(IWC), with a section cut away. The e ect of anisotropic mixing can be seen in the lower horizontal layer, fall streaks are observed on the vertical surfaces and the top layer has a convective appearance.

4.8.1 Validation of the fall streak structure

The fall streak pattern predicted using the UM winds is visualised in the vertical plane of motion of the generating cell over the radar. For the cloud of 27 December 1999, little di erence is seen between the projection onto the direction of advection and the cross-section along the x-axis, because the wind was almost directly from the west and the fall streaks are ideally aligned. The projection would be important if there was significant change in the wind direction with height. The projected fall streak line is superimposed on the radar image of the height-time Z field for comparison. An example of such a plot is shown in figure 4.14. If the projected fall streak is clearly out of line with those in the radar image, either the model generating level height is

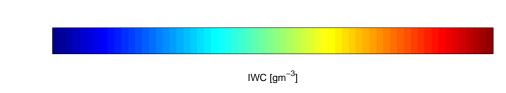


Figure 4.14: Verifying the height of the generating level and fall streak geometry. The yellow lines, superimposed onto the radar-derived IWC field, are the geometry predicted by the model using the UM wind profiles and a generating level of 8 km. Good agreement is obtained in the lower 2 km of the cloud. Above the generating level, the match is reasonable but not as close, due to the assumption of constant fall speed and inaccuracies in the UM wind profile.

not close to its true level or the fall speed profile needs to be adjusted. If a constant fall speed is assumed, altering the magnitude will simply stretch the section of the fall streak beneath the generating level horizontally by factor (old speed/new speed).

As the wind shear is more or less constant and we have assumed a constant fall speed, the form of the fall streaks below the generating level is near-parabolic. If

the true variable fall speed profile were to be used (this information can now be obtained from the Galileo 'Doppler velocity' facility which was not available at the time relevant to the data sets investigated here), there would be a departure from parabolic behaviour, and would increase chances of a closer agreement between the modelled and observed fall streak structures. Changing the generating level height however, may lead to a di erent fall streak structure, see figure 4.15. Note that it might not be possible to achieve a perfect match between the model and radar plots because the wind component vertical profiles come from the UM forecast data, which although are remarkably accurate (Mittermaier *et al.*, 2003), will not be completely reliable, in the vicinity of fronts, for example. Also, only one generating level can be assumed, whereas in reality the generating level may well be a function of horizontal position due to local turbulence and/or development of the weather system.

4.8.2 Verification of the spectral slopes

Power spectra of the model In(IWC) field are plotted to verify that the 1D spectral behaviour is reproduced. For each vertical level, 1D spectra are calculated for each row parallel to the *x*-axis (ideally the *x*-axis will be aligned with the wind direction of the generating level) and are then averaged in the *y*-direction. The averaged spectrum is taken to be representative for that particular height. In this way, noise is reduced and the spectral slope can be more precisely determined.

The slope of each spectrum is calculated as before. The lines of best fit are superimposed to check that the range for the fit is suitable. An example is shown in figure 4.16. Plots of the spectral slope as a function of height using (a) the model and (b) the radar observations are shown in figure 4.17 for comparison. Very close agreement is evident. The same figure also illustrates the curves obtained using

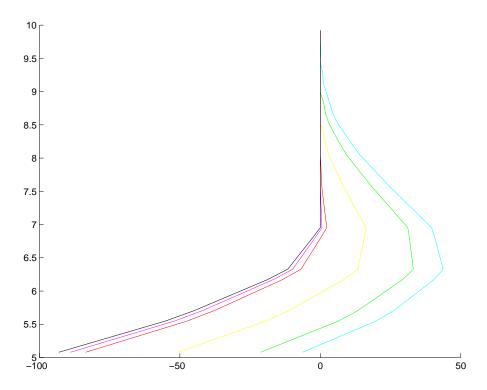


Figure 4.15: Computed fall streak structure for various generating levels between 6.5 and 9.5 km. The generating level height for each fall streak is specified by the key.

various approximations of the mean spectral energy density discussed in section 4.2.

4.8.3 Verification of the e ect of anisotropic mixing

The spectral slope as a function of height will be a ected by the anisotropic mixing. To verify that the correct slope is attained, the 1D spectrum for each height must be analysed in the direction of the wind shear at the same height. The simplest way to check the functioning of the code is to create a wind profile with v = 0, where v is the component of the wind in the y direction, and compare the spectral slope given by the model and the slope given by the observations as before. For the observed cloud, the wind lies mainly in the E-W direction and the anisotropic mixing is seen

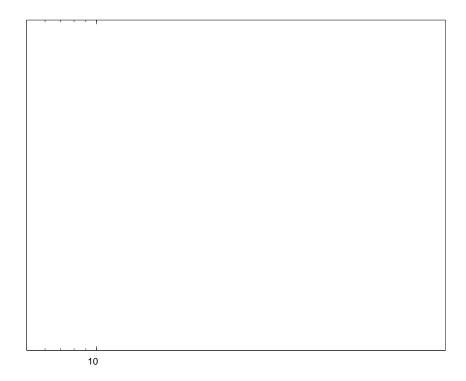


Figure 4.16: A sample power spectrum (red) of In(IWC) produced by the model for the height 6.02 km. A smoothed spectrum obtained by averaging over equal sections of log(k) is shown in black. A least squares regression (dashed blue line) is used to determine the spectral slope. The smoothed spectrum obtained from the radar observations at 5.91 km (the closest observed height to 6.02 km) is overplotted (dotted black line).

to have the correct e ect in figure 4.18. We obtain close to the requested slope in the direction of mixing, and there is also a 'bleed-though' e ect in the perpendicular direction.

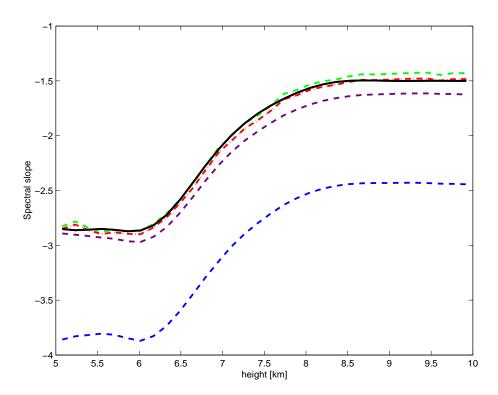


Figure 4.17: The spectral slope obtained from the radar data analysis (black) is compared to the spectral slopes produced by the model for the height range of the cloud. Shown in blue is the slope obtained using the isotropic assumptions. The improvement obtained by considering the adjustment to E_3 when $k < k_z=2$ is plotted in purple. The green line shows further improvement in using the analytic solution of equation 4.8 for $k > \max k_x$. The red line is the slope obtained by applying the full numerical solution in place of the analytic solution, and is the slope that we finally chose.

4.9 3D visualisation

To summarise, a stochastic model has been created that is able to simulate realistic 3D cirrus clouds, for the first time. The flexibility to specify alternative input values

Figure 4.18: Testing the anisotropic mixing. In the direction of mixing the requested slope is obtained. Perpendicular to the direction of mixing (in the horizontal plane), the change in slope is about half of the requested change.

means that the model can decouple from the radar data analysis and be used for idealised studies.

A three dimensional model allows the full fall streak to be resolved, if the wind shear profiles are known, whereas the observations from Galileo are limited to two dimensions. The 3D structure is visualised in figure 4.19 by plotting a surface defined by Z = i 5 dBZ. Height is colour graded for clarity.

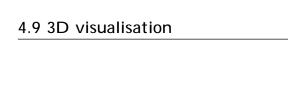


Figure 4.19: A three dimensional view of the fall streaks, using the Z=j 5 dBZ surface. The colour-grading of the field represents height, and is just for clarity.

53

Chapter 5

Radiative properties of fractal cirrus

In this chapter, we consider and investigate how domain-averaged radiative fluxes are related to particular inputs to the fractal model which exert influence over cloud inhomogeneity. We introduce the radiation scheme used and then describe the various cloud fields presented to the scheme.

5.1 The radiative transfer code

As discussed in the introduction, the e ects of cloud inhomogeneity may be divided into two parts:

- 1. The e ect of inhomogeneity due to variations in optical depth.
- 2. The e ect of horizontal photon transport.

Investigations of the second e ect, which would require use of a 3D Monte Carlo radiative transfer scheme, will be the focus of future studies. For now, we turn our

attention to the first e ect, which may be quantified using the plane-parallel bias. The plane-parallel bias is the di erence between a domain-averaged radiative property calculated using the independent column approximation (ICA) and that calculated using the plane-parallel (PP) approximation. We use the Edwards-Slingo radiative transfer scheme (Edwards and Slingo, 1996) to calculate the radiative fluxes for both the PP and the ICA assumptions and, in addition, we simulate a GCM calculation.

5.1.1 The Edwards-Slingo radiation scheme

The Edwards-Slingo (ES96) scheme is used operationally in the Met O ce Unified Model to calculate longwave (LW) and shortwave (SW) fluxes and heating rates for 1D atmospheric profiles. In this study, it is used to calculate domain averaged fluxes assuming the independent column approximation (ICA). The code is run over each column of the model-producedmo longw the T/F211.95 imeating eeco Edw sce Reeac

- 9. solar zenith angle
- 10. surface emissivity
- 11. surface albedo.

Inputs 1-4 are obtained from the latest UM forecast for the relevant date and time. The IWC profile is given entirely by the fractal cloud model. Above and below the cloud boundaries, the IWC is zero. UM inputs 1-4 are interpolated to the grid of the fractal cloud model over the vertical range of the cloud. Above and below the cloud, the UM grid remains in use. We assume a constant e ective radius, of 50 ⁷m for simplicity, although it would be possible to introduce a more realistic e ective radius profile into the 3D fractal cloud model. E ective radius can be related to temperature (Kristjánsson *et al.*, 2000), and to IWC (Evans and Wiscombe, 2003). The cloud fraction is taken as unity for all the heights in a profile for which IWC > 0, and the solar zenith angle is set 60°. The surface emissivity is assumed to be 1 and the surface albedo is assumed to be 0.2. The code is run twice for each profile. The first run is for the LW spectral region, and the second is for the SW.

5.1.2 Approximations

Although the code takes only 1.2 seconds to compute a single profile on a Sun workstation, a 128 £ 128 grid will take approximately $5\frac{1}{2}$ hours to produce results. To reduce the run-time, we can present the radiation code with a reduced IWC field by doing some horizontal averaging of the high resolution IWC fractal field. The field is averaged over every 4£4 grid cells in a horizontal plane, generating a 32£32 grid. A sensitivity test is carried out to see if there is structure at scales smaller than the new grid spacing which is significantly influencing the radiative transfer. Unfortunately,

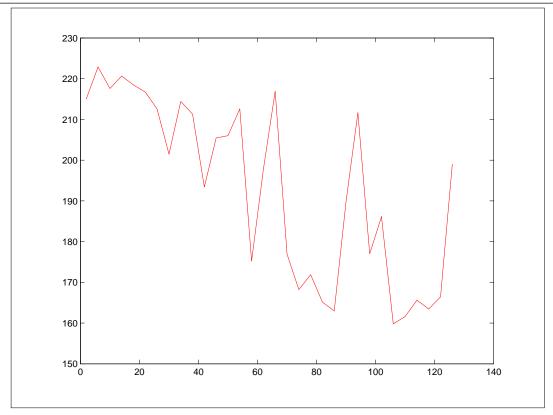


Figure 5.1: Sensitivity test to determine whether small scale variations, which are smoothed out in the reduced resolution grid, have a significant e ect on radiation. The upwelling LW radiation of one row (1£32 cells) of the 32£32 reduced field is shown in red. This row size corresponds to a 4£128 strip of cells at the high resolution. The blue dotted line shows the upwelling LW flux which has been averaged over the width of the strip. A good deal of smaller scale variability can be seen along the length. When this is averaged over every 4 cells along the length of the strip (green line), we see that the LW flux produced by the higher resolution grid is consistently larger than that produced by the low resolution grid.

5.2 Cloud fields

Since wind shear is very much responsible for the fall streaks which characterise cirrus cloud geometry, we chose to investigate the e ect of shear on domain-averaged radiative properties of cirrus. We also investigate the e ect of di erent isotropic

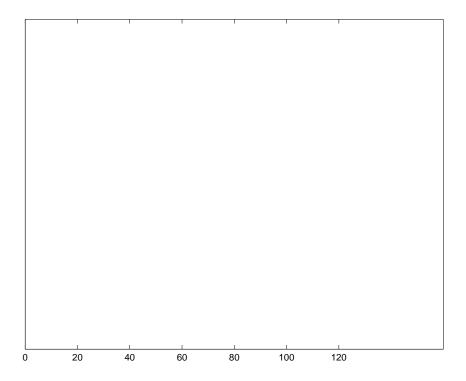


Figure 5.2: A scatter plot of reflectance (i.e. SW albedo) against optical depth for a typical radiation calculation. The SW albedo given by the empirical formula is overplotted: albedo = $0.232 + \frac{0.52}{2+3}$.

spectral slopes. Initially we will carry out all tests using the same set of random numbers to generate the initial fractal, to be sure that any changes in radiative properties result from the wind shear or spectral slope and nothing else. The radar observed cloud of 27 December 1999 is not used for these investigations as it is physically and optically thick and the LW and SW fluxes reach their saturation levels. In addition, the generating level for this cloud was found to be 2 km below the cloud top and most of the solar radiation is attenuated in these top layers before the e ect of shear, which occurs predominantly in the lower 2 km of the cloud, has chance

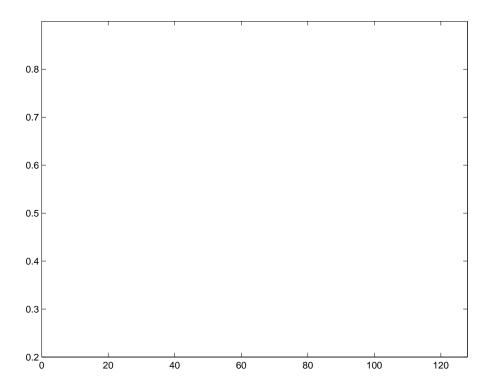


Figure 5.3: Comparison of the SW albedo given by the Edwards-Slingo (1996) radiation scheme and the empirical formula.

to show. It is the physically and optically thinner clouds that should demonstrate the e ect of inhomogeneity on radiative transfer in the mid-latitudes (Del Genio, 2001), because their optical depth range is mainly in the region of curvature of the albedo-optical depth relationship. We can see this from examining figure 5.2. Above a certain range of optical depths (≥ 10), the albedo or OLR is near reaching a saturation level. We therefore experiment with a thinner cloud. For simplification we choose to use idealised profiles of IWC and wind shear, but other parameters are based on the cloud of 27 December 1999.

The profile of mean IWC, which takes a constant value of 0.05 gm⁻³ except at the cloud edge where it is reduced smoothly to zero, and the e ective radius, r_{e_i} are

5.2.1 GCM resolution simulation

To demonstrate the inadequacy of the representation of cirrus cloud inhomogeneity in a GCM, we simulate a GCM representation of the cloud fields created by the 3D model, and compare the results of the experiments. A GCM grid box will contain a cloud fraction and, in the cloudy part of the box, each horizontal layer of the cloud is assumed to be uniform. An overlap assumption is required to determine how a layer is placed with respect to its neighbours. The simplest approach, the one employed by most GCMs, is to assume 'maximum random' overlap (Hogan and Illingworth, 2000). Maximum overlap is assumed between adjacent GCM cloud layers if the cloud is vertically continuous, and random overlap is applied to clouds at di erent heights if they are separated by a completely cloud-free layer. In this study, the cirrus cloud fields created are vertically continuous and so random overlap would not have been employed by a GCM. Maximum overlap alone is therefore assumed. In each layer, the cloudy grid cells are shifted to the same side of the GCM grid box (figure 5.5).

Most GCMs use atmospheric pressure as their vertical coordinate, so their vertical

5.3 Results 64

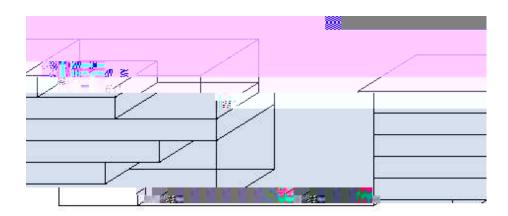


Figure 5.5: Schematic illustration of the 'maximum overlap' assumption used for vertically continuous clouds in a GCM. The cloud filled fractions for each layer are piled up at the same end of the grid box.

5.3 Results 65

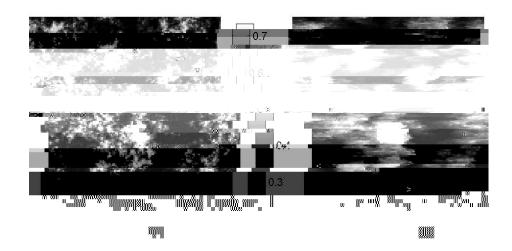


Figure 5.6: The SW albedo fields for wind shears of (a) 0 s^{-1} and (b) 0.006 s^{-1} looking down from above. The domain size is 200 km by 200 km. The colour key scale of SW albedo applies to both fields.

5.3.1 The top-of-the-atmosphere domain-averaged SW albedo

The SW albedo referred to in this section is the ratio of the domain-averaged SW upwelling flux to the domain-averaged SW downwelling flux at the top of the atmosphere. The SW albedo is displayed in figure 5.7 as a function of the wind shear for the three spectral slopes investigated. The results from the GCM simulation are shown in the same figure.

The SW downward flux is constant for all the experiments, as the solar zenith angle, date and time are held constant, and takes a value of 684.8 Wm⁻². Multiplying the SW albedo by the SW downward flux gives SW upwelling fluxes of 273.4 Wm⁻², 277.2 Wm⁻² and 282.5 Wm⁻² at the maximum wind shear of 0.048 s⁻¹ for the spectral slopes of i 8=3 i 5=3 and i 1 respectively. The minimum albedo of 0.33 (zero shear, slope = -8/3) corresponds to SW flux of 226.7 Wm⁻².

The plane-parallel SW albedo found by inserting the domain averaged optical

Figure 5.7: Dependence of SW albedo on magnitude of wind shear (constant with height). Results are shown in blue for the full 128£128 column cloud field with a spectral slope of -5/3, in red for a spectral slope of -8/3 and in green line for a slope of -1. The same colour coding applies to the dashed lines which give the results from the GCM simulation. The black line shows the limiting plane-parallel SW albedo.

depth, $\angle = 3.164$, into the empirical formula for albedo, and given in equation 5.1 is 0.4887. This is equivalent to an upwelling flux of 334.7 Wm². The albedo estimated using the plane-parallel approximation is indicated by the horizontal black line in figure 5.7. The plane-parallel bias, (i.e. the PP albedo minus the ICA albedo) is largest for the case of no shear, indicating that this is the cloud configuration furthest removed from the PP approximation. For the three di erent slopes it takes the values of 0.158 (slope = -1), 0.157 (slope = -5/3) and 0.128 (slope = -8/3), which

are very similar to the biases of 10-15% found by Cahalan (1994) and Barker and Davies (1992). This can be expected as there is little or no shear in stratocumulus and the cloud altitude has little e ect on the SW fluxes. The PP bias is about 8% (slope = -5/3) for the largest shear. Carlin *et al.* (2002) reported a range of cirrus solar albedo biases of up to 25% which were dependent on solar zenith angle (SZA) and underlying surface albedo. For an SZA of zero (which should be similar to our ICA approximation) they calculated albedo biases of a few percent, which compares favourably with our results.

We can see that GCMs capture some of the vertical inhomogeneity and can improve their estimate of domain averaged-albedo with respect to the PP albedo as a consequence of including a cloud fraction for each of their vertical levels.

The SW albedo increases as the cloud configuration becomes more sheared and consequently more similar to the PP form. This is a consequence of the non-linearity of the albedo-optical depth relationship, (see figure 1.1). For each wind shear experiment we see that as the spectral slope steepens, the SW albedo is reduced. Barker and Davies (1992) observed the same trends when they carried out a similar experiment for stratocumulus clouds. Their data were obtained using 2D isotropic, scaling, broken cloud fields. They investigated the relationship between spectral slope and reflectance (SW albedo) testing slopes between 0 and 4, for a solar zenith angle of about 78°. They held constant the cloud fraction (equivalent in this study to constant wind shear) and the domain-averaged optical depth. Their cloud fields, however were input to a Monte Carlo photon transport code, rather than a 1D ICA radiative transfer scheme. They showed that as the spectral slope steepens, the SW albedo tends to a 'plane-parallel' limit which they defined as $R_{pp} \not\in A_c$, where R_{pp} is the plane-parallel reflectance (SW albedo) and A_c is the cloud fraction.

5.3.2 The top-of-the-atmosphere domain-averaged upwelling LW radiation

The results for the upwelling LW fluxes are shown in figure 5.8. The colour coding used in figure 5.7 also applies here. The general trend is that the upwelling LW radiation decreases as wind shear increases and as the spectral slope becomes more shallow. The upwelling LW flux is greatest when there is no wind shear. This flux magnitude is enhanced due to the broken cloud field which allows more LW flux to reach the top of the atmosphere without being intercepted by the cloud. The gradient of both the SW and LW radiative properties tends to flatten with increasing wind shear. This is because the wind shear causes the fall streaks to become more horizontal and therefore the cloud optical depth must become more horizontally homogeneous. The PP upwelling LW flux estimate is 149.0 Wm⁻². The maximum PP biases of upwelling LW flux range from 23 to 36 Wm⁻² (slope = -1), and 36 to 53 Wm⁻² (slope = -8/3). Fu *et al.* (2000) reported cirrus PP biases, for the LW upwelling flux, which spanned a greater range.

The height of cloud base and depth of cloud will influence the upwelling LW flux as the flux emitted by a radiating body (which in the case of clouds is in the LW part of the spectrum) has a T^4

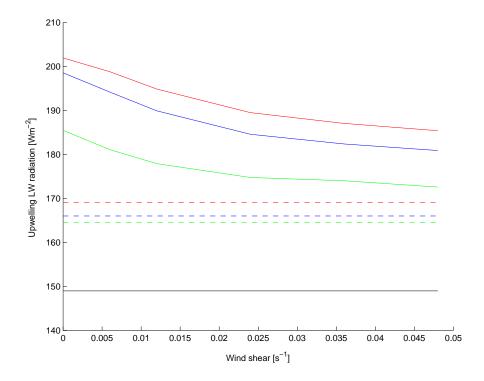


Figure 5.8: Dependence of upwelling LW radiation on magnitude of wind shear (constant with height). The blue line shows results for a cloud field with a spectral slope of -5/3. The red line is for a spectral slope of -8/3 and the green line is for a spectral slope of -1. The same colour coding applies to the dashed lines which give the results from the GCM simulation. The black line shows the limiting plane-parallel LW Upwelling flux.

there will be little or no contribution from the SW fluxes and the LW warming e ect will dominate. To gain an understanding of the net e ect of cirrus inhomogeneity on warming or cooling, many more cases would need to be investigated. The radiative fluxes will be dependent on numerous variables, such as the domain-average optical

tral mixing in the horizontal plane. Height dependent statistics such as the mean IWC, and the standard deviation of In(IWC) are based on vertically pointing 94 GHz radar observations of one particular mid-latitude cirrus cloud, chosen because the fall streaks were ideally aligned with the direction of motion of the cloud across the radar. The Unified Model vertical profiles of wind and temperature were also important input parameters in determining the IWC from radar reflectivities and the fall streak structure.

Observations of the dependence on the 1D spectral slope on height were particularly intriguing. At cloud top, the spectral slope is constant with height (about -4/3), until the generating level is reached. The slope below this height gradually steepened, reaching values of around -3. Various spectral slopes over a similar range have previously been reported but without mention of the dependence of the scaling exponent on height, or any other parameter. In this study we assume that the change can be attributed to mixing due to fall streaks intersecting and/or varying ice crystal fall speeds.

Limitations of the model have already been discussed at various points of this report. They include reliability on the accuracy of UM wind profiles. This would be required if the model were to be used in the interpretation of 2D satellite images to estimate the third dimension of the cloud field. It would not be so important in the application of the model to radiative transfer investigations where it is often more instructive to use a generalised or idealised shear. Three main assumptions were outlined in the introduction, that of a constant e ective radius (50 ¹m), a lognormal PDF for the IWC and a constant generating level. The Galileo radar has now been Dopplerised, allowing fall speeds and sizes of precipitation particles to be determined. The next stage of development could include the implementation

of a height dependent fall speed profile and a height dependent PDF for ice crystal e ective radius. There has already been some research into the later, for example, Evans (2001) produces a stochastic field for the particle e ective radius by using a height (which is related to temperature) and LWC dependent lookup table operating on a Gaussian field. This ensures that appropriate values of r_e are produced for each LWC value, so that for example, $r_e = 0$ does not occur inside of clouds.

Many further radar observations should be examined in order to verify trends which have been observed for the 27 December 1999. For example, in Hogan and Illingworth (1999) we noted an outer scale of 25 km for cirrus, but our cirrus cloud data from 27 December 1999, indicated an outer scale of about 60 km. If anisotropic mixing truly occurs in the direction of the fall streak orientation then, the measurement of outer scale will be dependent on the alignment of the fall streaks with the

Appendix A

Ice Fall Streak Geometry

Consider the top of a cirrus fall streak as a 'generating cell' which moves with the wind at that height and releases crystals. The 3D shape of the fallstreak is found by considering the trajectory of a single crystal as it falls, in the frame of reference of the generating cell.

Marshall (1953) derives the trajectory of the ice crystals as follows: If x represents distance in a particular horizontal direction, z is the depth (vertical distance increasing downwards), $u(z) = \frac{dx}{dt}$ is the component of the wind in the x direction and the fall speed $w(z) = \frac{dz}{dt}$ then the equation of the ice particle trajectory can be described as

$$x_{j} x_{0} = \int_{0}^{Z} \frac{u(z)}{w(z)} dz;$$
 (A.1)

where x_0 is the x coordinate of the generating element. Marshall (1953) examines the case when wind shear and fall speed are both constant. With u = Sz and w = b, where S and b are both constants (and S is the shear), equation A.1 simplifies to

$$x_i \quad x_0 = \frac{S}{2h} z^2; \tag{A.2}$$

which describes a parabola.

The pattern formed by ice particles precipitating from the generating cell is the trajectory of the particles, in the frame of reference of the generating cell. In any other frame of reference, the pattern and trajectory become two dierent things.

We would like to find the fall streak geometry for any wind shear scenario. To work in the reference frame of the generating cell we replace u(z) in equation A.1 by $u(z)_i$ $u(z_t)$ where z_t is the generating level height and $u(z_t)$ is the velocity component in the x direction at that height. Let $x_0 = 0$ and allow x to represent the horizontal displacement between a crystal and the generating cell, such that

$$X(Z) = \sum_{z'=z}^{Z'=z_t} dX = \sum_{z'=z}^{Z'=z_t} \frac{u(z') \, j \, u(z_t)}{w(z')} dz' \, . \tag{A.3}$$

Similarly, if y represents horizontal displacement relative to the generating cell and perpendicular to x, and $v(z) = \frac{dy}{dt}$, then

$$y(z) = \sum_{z'=z}^{Z} \frac{z'=z_t}{z'=z} dy = \sum_{z'=z}^{Z} \frac{v(z') j v(z_t)}{w(z')} dz':$$
 (A.4)

If we know the profiles of u_i , v_i and w_i , at heights z_i from levels i = 0 to i = tat the generating level, which must also be known, then equations A.3 and A.4 can be solved iteratively using finite di erences. We set $x_t=0$ and $y_t=0$ and work downwards from the generating level using the following iterations,

$$x_{i} = x_{i+1} + \frac{\mu_{i+1} + u_{i}}{2} \int_{i}^{y} u_{t} (z_{i+1} \int_{i}^{y} z_{i}) \frac{2}{w_{i+1} + w_{i}}$$

$$y_{i} = y_{i+1} + \frac{\nu_{i+1} + \nu_{i}}{2} \int_{i}^{y} v_{t} (z_{i+1} \int_{i}^{y} z_{i}) \frac{2}{w_{i+1} + w_{i}}$$
(A.5)

$$y_i = y_{i+1} + \frac{\mu_{i+1} + \nu_i}{2} j \quad v_t (z_{i+1} j \quad z_i) \frac{2}{w_{i+1} + w_i}.$$
 (A.6)

If the fall speed w_i is unknown, a constant value could be assumed. Typical fall speed is about 1 ms⁻¹ (e.g. Mittermaier *et al.* (2003), Marshall (1953), Heymsfield (1975)).

The fall streak geometry can then be approximated in the model by shifting each horizontal slice with respect to the slice at generating level height by $(\pm x, \pm y)$, where for slice i,

$$\pm X_i = X_i j \quad X_0 = X_i$$
; and $\pm y_i = y_i j \quad y_0 = y_i$:

Appendix B

Treatment of incomplete data sets

This appendix describes how to find the mean and standard deviation for broken data sets assumed to have a Normal PDF. It is credited entirely to Robin Hogan but is included here for the sake of completeness.

Suppose we have a series of data values x, which in the context of this study could represent radar reflectivity in dBZ, or $\ln(IWC)$ for which we would like to estimate the mean and standard deviation. Due to the sensitivity of the radar, there are missing values in the series where all we know is that $x < x_c$, where x_c is the minimum detectable signal. We suppose that the underlying probability density function (PDF) is a Normal, with mean x_m and standard deviation \mathcal{X}_x . We know the fraction f of the data series for which a valid value has been recorded (i.e. the fraction of the underlying PDF for which $x > x_c$) and the mean of these measured values x_m .

If we know x_c , x'_m , and f we can derive x_m and \mathcal{X}_x . The probability density function, P(x), is a Normal distribution:

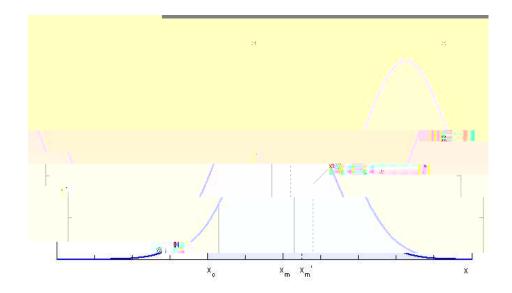


Figure B.1: The underlying Normal PDF of a broken data set x.

$$P(x) = P \frac{1}{2 \frac{\pi}{4} x} \exp^{\pi} i \frac{1}{2} \frac{\mu_{x} x_{i} x_{m}}{\frac{3}{4} x}$$
 (B.1)

Therefore, the detected fraction f is

$$f = \int_{x_c}^{Z} P(x) dx$$
 (B.2)

The standard integral of a Normal distribution, (x), is defined as

$$(x) = P \frac{1}{2 \frac{\pi}{4}} \int_{-\infty}^{Z} \exp \left(\frac{\tilde{A}}{t^2} \right) dt$$
 (B.3)

Thus f is given by

$$f = \frac{\mu_{X_m j} X_c}{\chi_x}$$
(B.4)

Consider now the mean of the detected values of x, which we designated x'_m ,

$$X'_{m} = \frac{\overset{R}{\underset{\infty}{\sim}} xP(x)dx}{\overset{R}{\underset{\infty}{\sim}} P(x)dx}$$

$$= \frac{1}{f} P \frac{1}{2 \frac{1}{\cancel{4} \cancel{4}_{x}}} \overset{Z}{\underset{x_{c}}{\sim}} x \exp \left[i \frac{1}{2} \cdot \frac{x i x_{m}}{\cancel{4}_{x}} \right]^{2} dx:$$
(B.5)

Now, let $t = \frac{\overset{X}{\underset{\infty}{\sim}} x - x_{m}}{\overset{X}{\underset{\infty}{\sim}}}$. Then $dt = \frac{2}{\underset{\infty}{\sim}} \frac{x - x_{m}}{\cancel{4}_{x}} dx$ and $x dx = \frac{\overset{X}{\underset{\infty}{\sim}} 2}{\cancel{2}}$

References

- Barker, H. W. and Davies, J. A., 1992: Solar radiative fluxes for stochastic, scale-invariant broken cloud fields. *J. Atmos. Sci.*, **49**, 1115-1125.
- Cahalan, R. F. and Joseph, J. H., 1989: Fractal statistics of cloud fields. *Mon. Wea. Rev.*, **117**, 261-272.
- Cahalan, R. F. and Snider, J. B., 1989: Marine stratocumulus structure. *Remote Sens. Environ.*, **28**, 95-107.
- Cahalan, R. F., Ridgeway, R., Wiscombe, W. J. and Bell, T. L., 1994: The albedo of fractal stratocumulus clouds. *J. Atmos. Sci.*, **51**, 2434-2455.
- Cahalan, R. F., 1994: Bounded cascade clouds: albedo and e ective thickness. *Nonlin. Proc. Geophys.*, **1**, 156-167.
- Carlin, B., Fu, Q., Lohmann, U., Mace, G. G., Sassen, K. and Comstock, J. M., 2002: High-cloud horizontal inhomogeneity and solar albedo bias. *J. Climate.*, **15**, 2321-2339.
- Cess, R. D.,

- Danne, O., Mace, G. G., Clothiaux, E. E., Dong, X., Ackerman, T. P. and Quante, M., 1996: Observing structures and vertical motions within stratiform clouds using a vertical pointing 94-GHz cloud radar. *Beitr. Phys. Atmos.*, 69, 229-237.
- Davis, A., Marshak, A., Cahalan, R. F. and Wiscombe, W., 1997: The Landsat scale break in stratocumulus as a three-dimensional radiative transfer e ect: Implications for cloud remote sensing. *J. Atmos. Sci.*, **54**, 241-260.
- Del Genio, A. D., 2001: GCM simulations of cirrus for climate studies. *Cirrus*, D. Lynch *et al.*, Eds., Oxford University Press, 310-326.
- Di Guiseppe, F. and Tompkins, A. M., 2003: E ect of spatial organisation on solar radiative transfer in three dimensional idealized stratocumulus cloud fields. Submitted to *J. Atmos. Sci.*.
- Edwards, J. M. and Slingo, A., 1996: Studies with a flexible new radiation code. I: Choosing a configuration for a large-scale model. *Quart. J. Roy. Meteor. Soc.*, **122**, 689-719.
- Evans, K. F., Mc Farlane, S. A. and Wiscombe, W., 2001: The importance of three-

- Heymsfield, A. J., 1975: Cirrus uncinus generating cells and the evolution of cirriform clouds. Part II: The structure and circulation of the cirrus uncinus generating head. *J. Atmos. Sci.*, **4**, 809-819.
- Heymsfield, A. J. and Mcfarquhar, G. M., 2001: Mid-latitude and tropical cirrus: Microphysical properties. *Cirrus*, D. Lynch *et al.*, Eds., Oxford University Press, 78-101.
- Hogan, R. J. and Illingworth, A. J., 1999: The potential of spaceborne dual-wavelength radar to make global measurements of cirrus clouds. *J. Atmos. Oceanic. Technol.*, **16**, 518-531.
- Hogan, R. J. and Illingworth, A. J., 2000: Deriving cloud overlap statistics from radar. *Quart. J. Roy. Meteor. Soc.*, **126**, 2903-2909.
- Hogan, R. J. and Illingworth, A. J., 2003: Parametrising ice cloud inhomogeneity and the overlap of inhomogeneities using cloud radar data. *J. Atmos. Sci.*, **60**, 756-767.
- Kristjánsson, J. E., Edwards, J. M., and Mitchell, D. L., 2000: Impact of a new scheme for optical properties of ice crystals on climates of two GCMs. *J. Geophys. Res.*, **105**, 10063-10079.
- Larson *et al.*, 2001: Systematic biases in the microphysics and thermodynamics of numerical models that ignore subgrid-scale variability. *J. Atmos. Sci.*, **58**, 1117-1128.
- Liu, C-L, and Illingworth, A. J., 2000: Toward more accurate retrievals of ice water content from radar measurements of clouds. *J. Appl. Meteorol.*, **39**, 1130-1146.

- Lovejoy, S., 1982: The area-perimeter relationship for rain and cloud areas. *Science*, **216**, 185-187.
- Lynch, D. K., 2001: Cirrus: History and Definition. *Cirrus*, D. Lynch *et al.*, Eds., Oxford University Press, 3-10.
- Marshall, J. S., 1953: Precipitation trajectories and patterns. *J. Meteor.*, **10**, 25-30.
- Mittermaier, M. P., Hogan R. J. and Illingworth, A. J., 2003: Exploring new synergies between radar data and mesoscale model forecasts. *Proc.* 31St AMS conf. on Radar Meteorol. Seattle, 6-12 August 2003
- Pincus, R., Barker, H. W. and Morcette, J., 2002: A fast, flexible, approximate technique for computing radiative transfer in inhomogeneous cloud fields. Submitted to *J. Geophys. Res.*
- Pomroy, H. R. and Illingworth, A. J., 2000: Quantifying bias in emissivity from radar observations. *Geophys. Res. Lett.*, **27**, 2101-2104.
- Press, W. H., 1992: *Numerical recipes in Fortran: The art of scientific computing.*Second edition. Cambridge University Press.
- Salby, M. L., 1996: Fundamentals of Atmospheric Physics. Academic Press, 36-46.
- Sassen, K., 2001: Cirrus clouds: A modern perspective. *Cirrus*, D. Lynch *et al.*, Eds., Oxford University Press, 11-40.
- Sassen, K. and Mace, G. G., 2001: Ground-based remote sensing of cirrus clouds. *Cirrus*, D. Lynch *et al.*, Eds., Oxford University Press, 168-196.

- Starr, D. O'C. and Quante, M., 2001: Dynamical processes in cirrus clouds: Concepts and models. *Cirrus*, D. Lynch *et al.*, Eds., Oxford University Press, 375-396.
- Stephens, G. L., 1988: Radiative transfer through arbitrarily shaped optical media. Part II: Group theory and simple closures. *J. Atmos. Sci.*, **45**, 1837-1848.
- Stephens, G. L. *et al.*, 2002: The CloudSat mission and the A-train. *Bull. Amer. Meteorol. Soc.*, **83**, 1771-1790.
- Tessier, Y., Lovejoy, S. and Schertzer, D., 1993: Universal Multifractals: Theory and observations for rain and clouds. *J. Appl. Meteorol.*, **32**, 223-250.
- Tiedtke, M., 1996: An extension of cloud-radiation parametrization in the ECMWF model: The representation of subgrid-scale variation of optical depth. *Mon. Wea. Rev.*, **124**, 745-750.
- World Meteorological Organisation (WMO), 1992: *International Meteorological Vo-cabulary. Second Edition.*, WMO no. 128, Geneva.